coatings

MDPI

Article

Acceptor-Enriched Charge-Transfer Engineering for Long-Life and High-Rate Organic Cathodes in Aqueous Proton Batteries

Xirui Song, Xinglin Yang *, Jinlong Yang, Weichao Zhang and Peixiang Shi

School of Energy and Power, Jiangsu University of Science and Technology, Zhenjiang 212003, China; 18012827367@163.com (X.S.); 15061256064@163.com (J.Y.); zhangweichao0302@163.com (W.Z.); 18361810297@163.com (P.S.)

* Correspondence: yangxl23320@163.com; Tel.: +86-1865-2867-102

Highlights

What are the main findings?

- An acceptor-enriched PNZ–TCNQ charge-transfer complex was fabricated and exhibited stable, reversible Faradaic behavior in an acidic aqueous electrolyte solution.
- The PNZ–TCNQ cathode delivered 10,000 cycles at 5 A g^{-1} with about 85% capacity retention, showing good high-rate and long-cycle performance.
- Spectroscopic analyses indicate reversible redox evolution of the donor–acceptor complex while preserving the main molecular backbone.

What are the implications of the main findings?

- The acceptor-enrichment strategy is beneficial for improving the electrochemical stability of organic charge-transfer complexes.
- The present results provide insight into how donor–acceptor assembly can be used to regulate the electrochemical behavior of organic cathodes in acidic aqueous systems.
- This work provides a useful strategy for developing organic cathodes for acidic aqueous energy storage.

Abstract

Aqueous proton batteries (APBs) are promising for safe energy storage, yet their cathode development is hindered by the lack of organic materials with reversible redox activity and long cycling stability in acidic media. Herein, an acceptor-enriched PNZ–TCNQ organic charge-transfer complex was constructed by increasing the TCNQ ratio. Spectroscopic results are consistent with strengthened donor–acceptor interactions and altered local electronic environments. The PNZ–TCNQ cathode delivered ~190 mAh g^{-1} at 0.6 A g^{-1} and retained ~85% capacity after 10,000 cycles at 5 A g^{-1} in acidic three-electrode tests. Kinetic analyses revealed mixed charge storage contributions from pseudocapacitive and diffusion-influenced processes. In situ/ex situ characterizations confirmed reversible redox evolution of the donor–acceptor complex with preserved molecular backbones. This work shows that tuning intermolecular charge-transfer interactions is an effective strategy for improving the cycling stability of organic cathodes in acidic aqueous electrolytes.

Keywords: aqueous proton batteries; organic charge-transfer; PNZ–TCNQ; reversible redox

Check for updates

Academic Editor: Octavian Buiu

Received: 6 March 2026
Revised: 30 March 2026
Accepted: 3 April 2026
Published: 6 April 2026

Copyright: © 2026 by the authors. Licensee MDPI, Basel, Switzerland. This article is an open access article distributed under the terms and conditions of the Creative Commons Attribution (CC BY) license.

1. Introduction

With the rapid development of renewable energy technologies and portable electronic devices, electrochemical energy storage systems are facing an urgent demand for high safety, low cost, and long service life. Although lithium-ion batteries currently dominate the commercial energy storage market, their reliance on flammable organic electrolytes, the limited and uneven distribution of lithium resources, and the associated potential safety risks severely restrict their further application in large-scale energy storage and complex operating conditions [1–3]. In contrast, energy storage systems based on aqueous electrolytes, featuring intrinsically high safety, good environmental compatibility, and high ionic conductivity, are widely regarded as an important development direction for next-generation safe energy storage technologies [4]. Among various aqueous energy storage systems, aqueous proton batteries (APBs) have attracted increasing attention in recent years. Unlike battery systems that employ Li^+, Na^+, or Zn^{2+} as charge carriers, APBs utilize protons (H^+) as the charge-transport species [5–8]. Protons possess the smallest ionic radius and the lowest mass, enabling faster insertion/extraction kinetics and lower structural strain within electrode materials [9,10]. More importantly, in aqueous environments, proton transport is not limited to conventional diffusion mechanisms but can also proceed through the hydrogen-bond network of water molecules via the Grotthuss proton conduction mechanism [11–13], in which protons undergo continuous hopping between neighboring water molecules through the breaking and reformation of hydrogen bonds [14]. This process significantly reduces the migration energy barrier and enables ultrafast ion transport. These characteristics make aqueous proton batteries attractive for high-rate electrochemical energy storage.

Despite these advantages, the practical development of APBs is still largely constrained by the selection and design of cathode materials. Ideal cathode materials for aqueous proton batteries should simultaneously exhibit reversible redox activity, favorable charge-transfer kinetics, and good structural stability in acidic aqueous electrolytes [15–18]. However, most cathode materials reported to date struggle to satisfy all these requirements concurrently. Currently, APB cathode materials can be broadly classified into three categories: metal oxides, Prussian blue analogues (PBAs), and organic materials [19–22]. Metal oxides (such as MnO_2, V_2O_5, and MoO_3) have been extensively investigated owing to their relatively high theoretical capacities, but they often suffer from dissolution, irreversible phase transitions, and poor cycling stability in acidic electrolytes [23–27]. PBAs, benefiting from their open three-dimensional framework structures, facilitate rapid ion diffusion and generally exhibit high coulombic efficiency; however, these materials typically lack mobile protons and require additional pre-protonation treatments, which increase synthesis complexity. Moreover, the presence of electrochemically inactive sites further limits their achievable capacity and energy density [28–31]. In comparison, organic electrode materials, characterized by high structural tunability, abundant resources, and redox-active functional groups, have gradually emerged as an important research direction for APB cathodes. Such materials can provide reversible electrochemical activity through conjugated frameworks and polar functional groups, while their molecular structures also offer broad opportunities for interfacial and charge-transport regulation. Nevertheless, most small-molecule organic materials still suffer from intrinsically low electronic conductivity and poor stability in aqueous electrolytes due to dissolution, resulting in limited rate capability and cycling durability [32–34]. To address these critical challenges, constructing organic charge-transfer (CT) complexes that simultaneously possess efficient electronic transport and structural stability has been proposed as an effective strategy [35,36]. Among them, tetracyanoquinodimethane (TCNQ), as a representative strong electron acceptor, features a highly conjugated planar structure and cyano-rich functional groups, enabling stabilization of its reduced states

during electrochemical processes and promoting intermolecular charge delocalization and π–π stacking, thereby exhibiting excellent redox activity [37–39]. However, pristine TCNQ or its simple derivatives still tend to dissolve and undergo structural instability in aqueous environments, which limits their direct application in aqueous proton batteries [40].

Herein, we report a novel aqueous proton battery cathode based on a PNZ–TCNQ organic charge-transfer complex. During synthesis, by rationally adjusting the reactant stoichiometric ratio and solvent conditions, a TCNQ-rich PNZ–TCNQ charge-transfer complex was constructed in an acetone system. This strategy promotes sufficient charge transfer between PNZ and TCNQ, thereby reducing uncomplexed components and improving the crystallinity and phase stability of the resulting material. Meanwhile, the introduction of a higher proportion of TCNQ enables its redox-active units to participate more effectively in the composite system, enhancing the utilization efficiency of active components within the electrode material. Furthermore, the charge-transfer interaction formed between PNZ and TCNQ induces redistribution of electronic density within the system, which improves the overall electronic transport properties of the composite and provides more efficient electron pathways for subsequent electrochemical reactions. Combined with the influence of the solvent environment on material formation, this synthetic strategy achieves synergistic optimization of the charge-transfer degree and structural characteristics. Through this study, we demonstrate a feasible pathway for regulating the electrochemical behavior of organic charge-transfer complexes via rational molecular combination and synthesis condition control, providing a new perspective for the exploration of cathode materials in aqueous proton batteries. Moreover, the results indicate that tuning intermolecular interactions in organic charge-transfer cathode systems plays a crucial role in governing proton-storage behavior and its kinetic characteristics, offering insights into the reaction mechanisms of organic cathode materials in aqueous proton batteries.

2. Materials and Methods

2.1. Material Preparation

PNZ (Phenazine), TCNQ (7,7,8,8-tetracyanoquinodimethane), and acetone were purchased from Aladdin (Shanghai, China). All commercially available chemicals were used as received without further purification. The synthesis of the PNZ–TCNQ charge-transfer complex followed the procedure described below. PNZ, TCNQ, and acetone were mixed at a molar ratio of 1:1.8:2.2 and stirred for 30 min at 40 °C. The resulting mixture was then vacuum-dried overnight at 40 °C. In contrast to previously reported protocols in which donor and acceptor monomers are mixed at equimolar ratios in acetone solution, increasing the amount of TCNQ facilitates more complete charge-transfer interactions, thereby improving the crystallinity and phase purity of the resulting complex. The acetone content also influences the crystallization rate and solvation degree; thus, adjusting the solvent ratio provides an effective means to regulate crystal growth.

2.2. Material Characterization

The morphology of the PNZ–TCNQ complex was characterized using scanning electron microscopy (SEM, ZEISS G500 Carl Zeiss AG, Oberkochen, Germany) and transmission electron microscopy (TEM, Tecnai G2 F20, FEI, Hillsboro, OR, USA). X-ray diffraction (XRD) patterns were collected using an X'Pert Powder diffractometer (Malvern Panalytical, Almelo, The Netherlands). In situ Raman spectroscopy was performed using a laser confocal Raman spectrometer (HR Evolution, Horiba, Kyoto, Japan). X-ray photoelectron spectroscopy (XPS) measurements were carried out on a Thermo Scientific ESCALAB Xi^+ system (Thermo Fisher Scientific, Waltham, MA, USA). In situ Fourier-transform infrared (FT-IR) spectroscopy was conducted using a Thermo IS50 spectrometer (Thermo

Fisher Scientific, Waltham, MA, USA). Nitrogen adsorption–desorption measurements were performed on an ASAP 2460 instrument (Micromeritics, Norcross, GA, USA) for Brunauer–Emmett–Teller (BET) surface area analysis. Liquid-state nuclear magnetic resonance (NMR) spectra were recorded on a BRUKER ASCENDTM 400 (MA, USA) spectrometer.

2.3. Electrochemical Measurements

The working electrodes were prepared by mixing PNZ–TCNQ, conductive carbon black (Ketjen black, Aladdin, Shanghai, China), and polyvinylidene fluoride (PVDF, Aladdin, Shanghai, China) binder at a mass ratio of 70:20:10 in N-methyl-2-pyrrolidone (NMP, Aladdin, Shanghai, China) to form a homogeneous slurry. The slurry was then coated onto carbon paper substrates and vacuum-dried overnight at 40 °C. An Ag/AgCl electrode and a graphite rod were used as the reference electrode and counter electrode, respectively, in a three-electrode configuration. A 2 M H_2SO_4 aqueous solution served as the electrolyte. Electrochemical impedance spectroscopy (EIS), cyclic voltammetry (CV), and galvanostatic charge–discharge (GCD) measurements of the half-cell were performed in the three-electrode system. EIS and CV measurements were conducted using a CHI 760E electrochemical workstation, while GCD measurements were carried out using a LAND battery testing system.

3. Results and Discussion

3.1. Structure of PNZ-TCNQ

Charge-transfer complexes are constructed through intermolecular electronic coupling between donor and acceptor molecules, forming solid-state assembled structures that provide a structural basis for reversible electrochemical reactions in aqueous proton batteries [41]. Different from the commonly reported construction strategies of PNZ–TCNQ systems, the present work deliberately increases the relative proportion of the TCNQ acceptor within the complex. This acceptor-enriched design is intended to enhance donor–acceptor interaction between the donor and acceptor units by leveraging the strong electron-withdrawing nature of TCNQ, thereby offering a structural modulation strategy distinct from previously reported approaches for tuning the electronic structure and solid-state packing behavior of PNZ–TCNQ complexes.

X-ray diffraction (XRD) analysis (Figure 1a) supports the successful construction of the PNZ–TCNQ charge-transfer complex. The experimentally obtained diffraction pattern is qualitatively consistent with the reference simulated pattern derived from the reported stacking model in the literature [40], while exhibiting diffraction features clearly distinct from those of pristine PNZ and TCNQ. This observation is consistent with the formation of a donor–acceptor assembled solid distinct from the pristine components. Meanwhile, the slight broadening of diffraction peaks may be related to the structural characteristics commonly observed in organic charge-transfer solids, such as relatively small crystallite size, lattice microstrain, or limited long-range order. Further Raman spectroscopic analysis (Figure 1b) reveals that the characteristic ring-vibration peaks of TCNQ in the 1400–1600 cm^{-1} region undergo a red shift in the PNZ–TCNQ complex, which is consistent with donor–acceptor interaction between the PNZ donor and the TCNQ acceptor. In the Fourier-transform infrared (FT-IR) spectra (Figure 1c), the PNZ–TCNQ complex retains a distinct –C≡N stretching vibration at approximately 2221 cm^{-1}, with no pronounced red shift compared to the pristine components, while noticeable changes are observed in the characteristic vibration bands in the 1500–1600 cm^{-1} region. These results suggest that the formation of the complex does not disrupt the molecular backbone structures of PNZ and TCNQ but instead is accompanied by changes in the local electronic environment through intermolecular interactions. X-ray photoelectron spectroscopy (XPS) analysis

(Figure 1d,e) further corroborates this conclusion from the perspective of chemical bonding environments. The C 1s spectrum can be deconvoluted into three characteristic peaks corresponding to C–C/C=C (284.6 eV), C–N/C=N (286.0 eV), and –C≡N (288.8 eV), where the presence of the –C≡N component confirms the effective participation of the TCNQ acceptor in the complex. In the N 1s spectrum, discernible shifts in nitrogen-related peaks relative to the pristine components indicate changes in the local electronic environment around nitrogen atoms, providing further evidence for intermolecular charge transfer between PNZ and TCNQ. Brunauer–Emmett–Teller (BET) analysis (Figure 1f) yields a specific surface area of 1.0758 m^2 g^{-1}, with the adsorption–desorption isotherm exhibiting features close to type IV behavior. The pore-size distribution is mainly concentrated in the 2–50 nm range, indicating the absence of significant intrinsic microporosity and suggesting that the observed mesopores originate primarily from interparticle voids formed during crystal packing rather than from a porous framework. Together with the low surface area, these results further indicate that PNZ–TCNQ is a dense organic complex crystal.

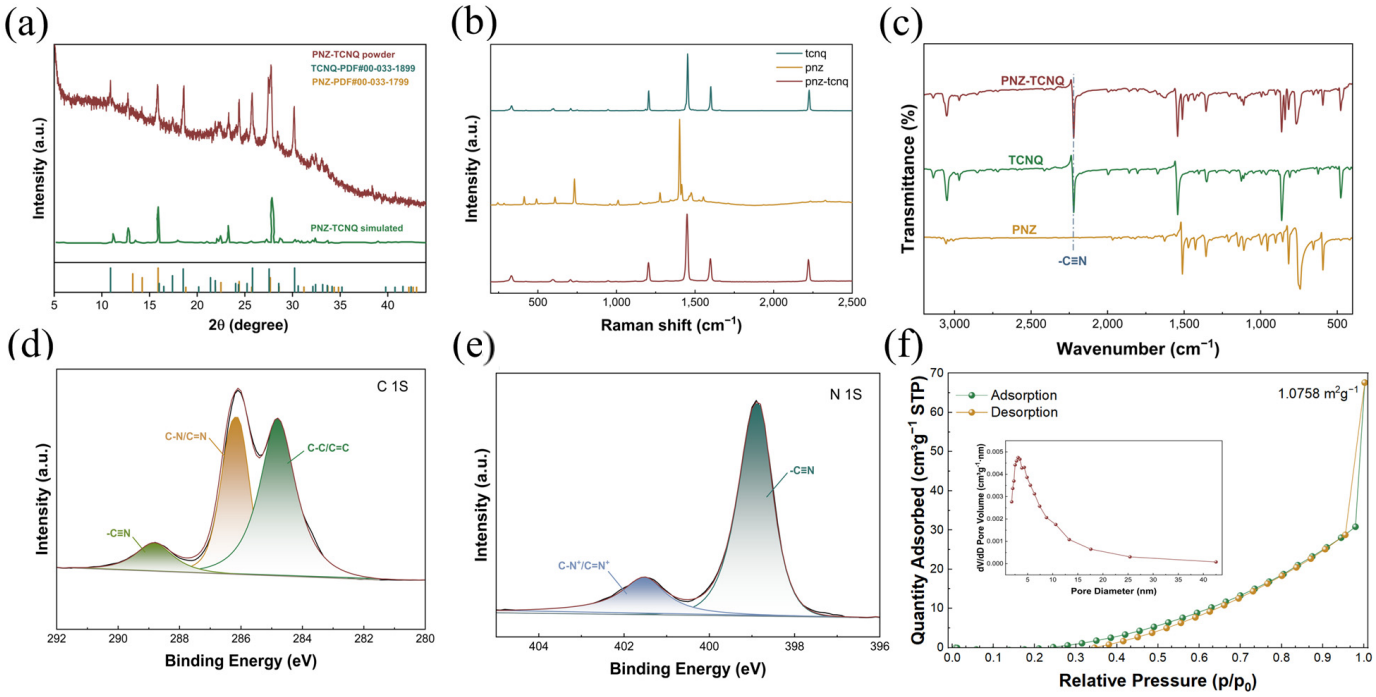

Figure 1. Structural characterization of PNZ-TCNQ: (**a**) XRD patterns; (**b**) Raman spectra; (**c**) FT-IR spectra; (**d**,**e**) XPS spectra; (**f**) Nitrogen adsorption–desorption isotherms and pore size distributions.

3.2. Morphology of PNZ-TCNQ

The microstructural morphology of the material was examined by SEM and TEM. As shown in Figure 2a,b, PNZ–TCNQ particles exhibit a generally regular polyhedral morphology with a relatively uniform size distribution, and local regions display a certain degree of ordered packing. TEM images further reveal that the particles possess a dense and homogeneous internal structure. SEM–EDS elemental mapping (Figure 2d) shows a uniform distribution of C, N, and O elements throughout the material, with C primarily concentrated within the particle body and N and O exhibiting consistent spatial distribution, indicating good compositional homogeneity. These results demonstrate that the material exhibits high consistency in both microstructure and elemental distribution, providing a reliable structural basis for investigating its electrochemical behavior in aqueous proton batteries.

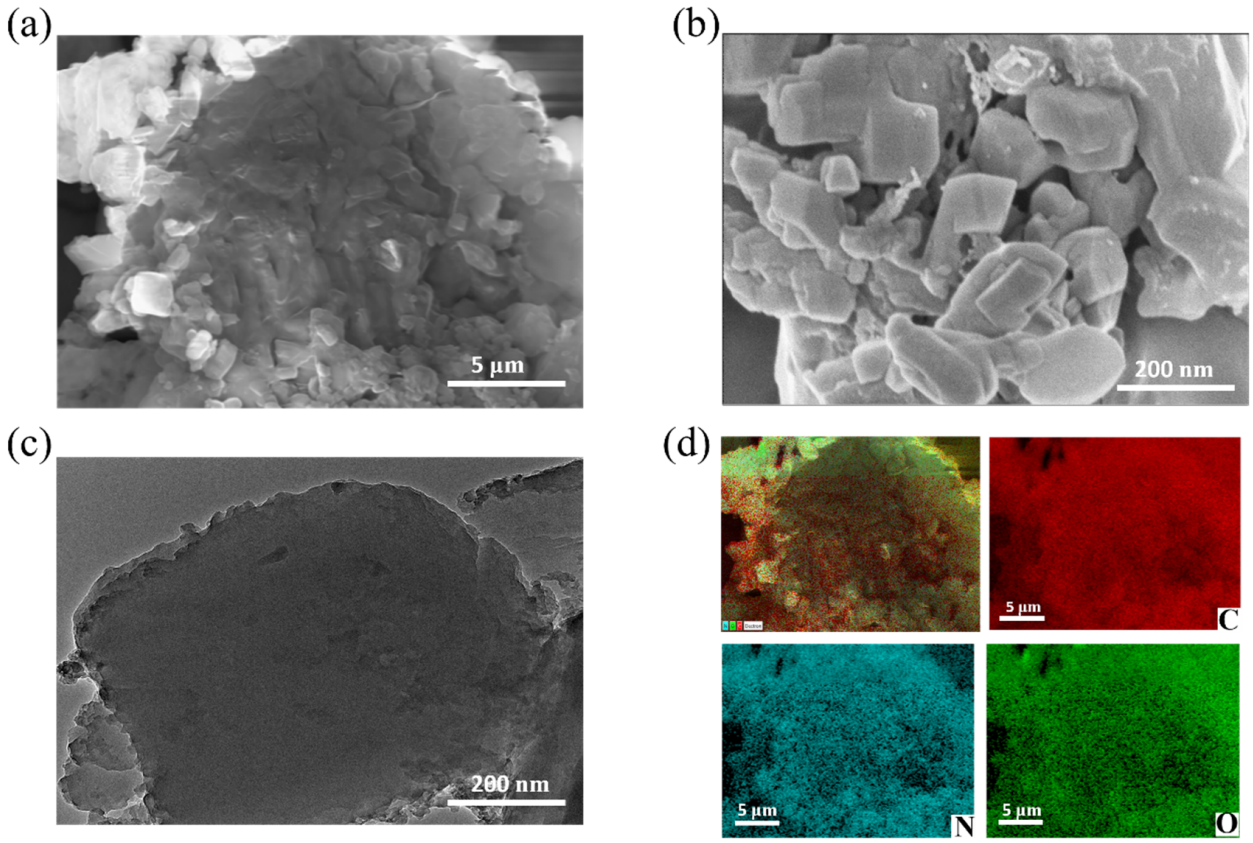

Figure 2. Morphological characterization of PNZ-TCNQ: (**a**) TEM image; (**b**–**d**) SEM image along with the corresponding elemental mapping images.

3.3. Electrochemical Performance

The electrochemical properties of PNZ–TCNQ were evaluated using cyclic voltammetry (CV) and galvanostatic charge–discharge (GCD) measurements in an acidic aqueous three-electrode system. As shown in Figure 3a, the CV curve recorded at a scan rate of 1 mV s^{-1} exhibits two distinct redox couples located at E_1 = 0.29/0.30 V and E_2 = 0.51/0.54 V versus Ag/AgCl. This dual-redox-feature behavior is consistent with the reversible redox characteristics of charge-transfer complexes formed through donor–acceptor intermolecular electronic coupling, indicating that the solid-state complex structure can continuously participate in Faradaic reactions under acidic aqueous conditions. From the second cycle onward, the CV curves largely overlap in both peak positions and overall profiles, reflecting good electrochemical stability of the redox processes during repeated cycling and providing a foundation for subsequent rate capability and cycling performance evaluations. Rate performance tests are presented in Figure 3b. When the current density is sequentially increased from 0.25 to 0.5, 1, 2, and 4 A g^{-1}, the electrode delivers discharge capacities of 213.6, 191.8, 167.4, 130.3, and 88.9 mAh g^{-1}, respectively. Upon returning the current density to 0.25 A g^{-1}, the discharge capacity recovers to 200.5 mAh g^{-1}, confirming good reversibility. At a current density of 0.6 A g^{-1} (Figure 3c), the PNZ–TCNQ electrode exhibits an initial discharge capacity of approximately 190 mAh g^{-1} and maintains a capacity of about 180 mAh g^{-1} after 200 cycles, corresponding to a capacity retention of approximately 94.7%. At a higher current density of 5 A g^{-1} (Figure 3d), the electrode sustains continuous cycling for up to 10,000 cycles, with an initial discharge capacity of 65.8 mAh g^{-1} and a capacity retention close to 85%. The active-material loading in this study is approximately 0.30 mg cm^{-2}. For comparison, a PNZ:TCNQ = 1:1 control sample was also examined, and its GCD response after 200 cycles at 0.6 A g^{-1} is less

favorable than that of the present PNZ–TCNQ electrode (Figure S3), indicating that the electrochemical behavior is sensitive to the donor/acceptor ratio. These results indicate that the charge-transfer complex maintains stable capacity output under high current densities and prolonged cycling, highlighting its potential for electrochemical energy storage applications requiring fast charge–discharge capability and long-term operational stability. In addition, the UV–vis spectrum of the post-cycling electrolyte does not show obvious new absorption features (Figure S2), suggesting that no evident large-scale dissolution of active species is observed under the present test conditions.

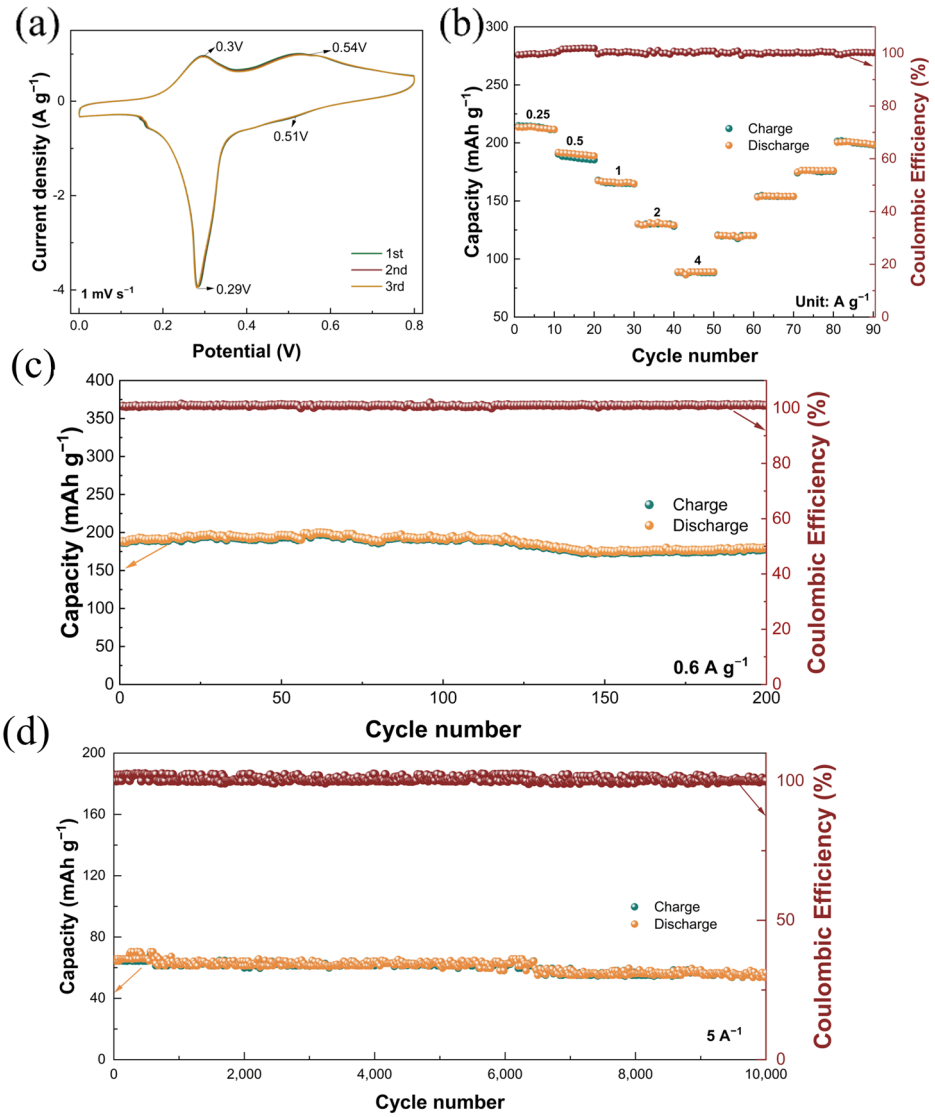

Figure 3. Electrochemical characterization of PNZ-TCNQ as cathode: (**a**) CV curves for the first three cycles recorded at 1 mV s^{-1}; (**b**) rate performance of PNZ-TCNQ at various current densities; (**c**,**d**) long-term cycling performance at 0.6 and 5 Ag^{-1}.

3.4. Kinetic Performance

To further analyze the electrochemical reaction kinetics of the PNZ–TCNQ electrode, CV measurements were conducted at various scan rates. As shown in Figure 4a, the CV curves recorded over a scan-rate range of 1–30 mV s^{-1} maintain well-defined redox features, with peak currents gradually increasing as the scan rate increases and only minor peak shifts observed, indicating good reversibility within the investigated rate range. The relationship between peak current (i) and scan rate (v) was analyzed using the power-law equation $i = a\ v^b$ (Figure 4b). The fitted b values (0.7–0.99) suggest

that the charge-storage process involves a combination of surface-related pseudocapacitive behavior and diffusion-influenced processes. Further quantitative analysis based on $i = k_1v + k_2v^{0.5}$ (Figure 4c) reveals that diffusion-related contributions remain significant at lower scan rates, while the pseudocapacitive contribution gradually increases and becomes dominant as the scan rate increases [42]. The corresponding capacitive contribution analysis (Figure S1) gives values of approximately 73%, 70%, 75%, 80%, and 95% at 1, 5, 10, 20, and 30 mV s^{-1}, respectively, further indicating that surface-related processes become increasingly important at higher scan rates. Electrochemical impedance spectroscopy (EIS) measurements were performed at different charge states, and the resulting Nyquist plots are shown in Figure 4d. All spectra consist of a semicircle in the high-frequency region and an inclined line in the low-frequency region, where the semicircle corresponds to the charge-transfer process at the electrode/electrolyte interface and the inclined line is associated with proton transport behavior. These features indicate that interfacial charge-transfer and ion-transport processes jointly contribute to the electrochemical reactions across different charge states. Combined with the distribution of relaxation time (DRT) analysis (Figure 4e), impedance contributions at different characteristic time scales can be distinguished, further confirming the coexistence of interfacial and diffusion processes during electrochemical operation. Together, these results demonstrate that the synergistic participation of pseudocapacitive behavior and diffusion-influenced processes enables PNZ–TCNQ to maintain favorable reaction kinetics over a wide range of operating conditions, providing an intrinsic kinetic basis for its stable performance during fast charge–discharge and long-term cycling.

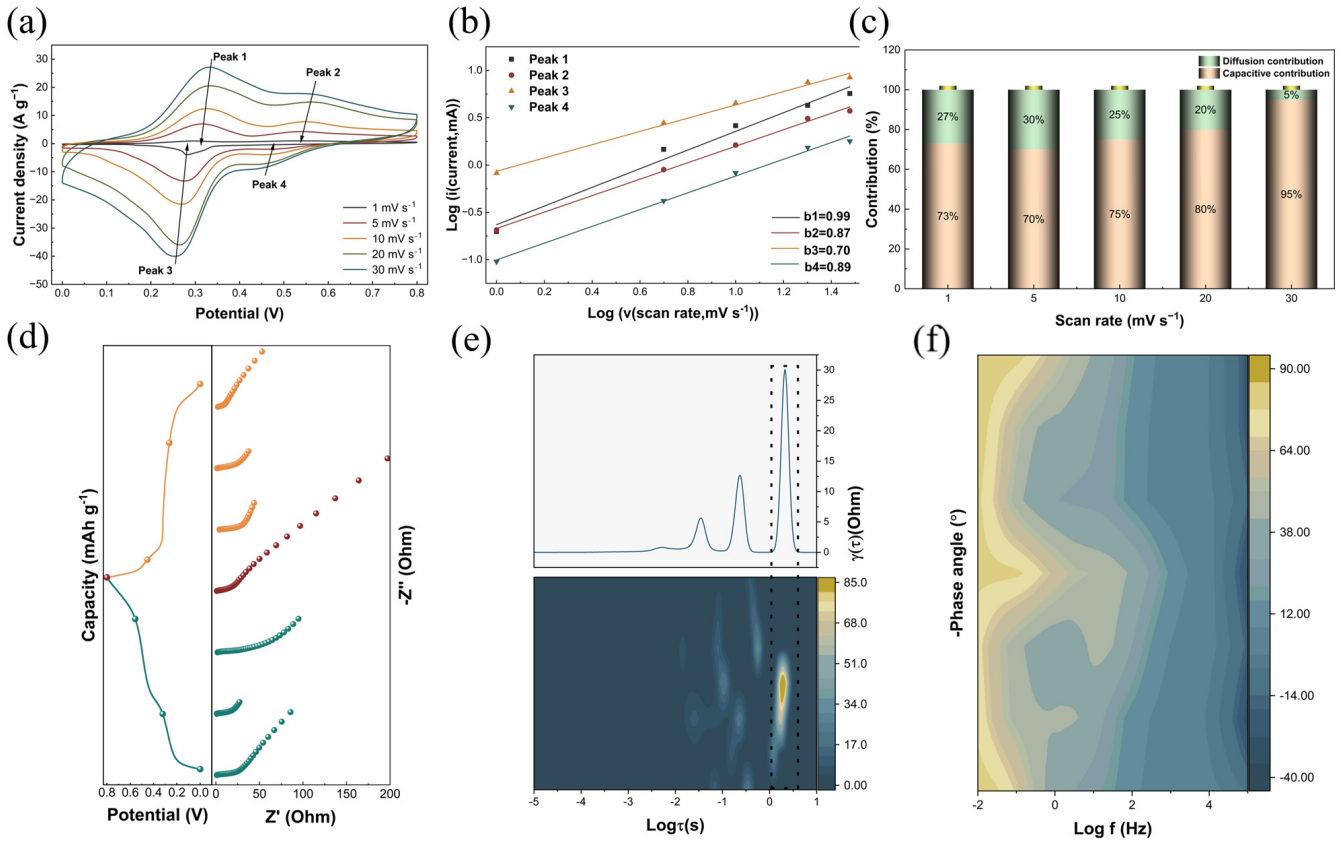

Figure 4. Electrochemical characterization of PNZ-TCNQ: (**a**) CV curves recorded at multiple scan rates; (**b**) Plots of ln(i) versus ln(v) for the corresponding redox peak currents; (**c**) Quantitative analysis of capacitive contribution at different scan rates; (**d**) EIS spectra measured at various states of charge; (**e**) Distribution of relaxation times (DRT) derived from the EIS data; (**f**) Bode plots at different applied potentials, illustrating frequency-dependent electrochemical behavior.

3.5. Mechanistic Analysis

To further elucidate the electrochemical reaction behavior of the PNZ–TCNQ complex during electrochemical operation, in situ Raman spectroscopy, ex situ FT-IR spectroscopy, and ex situ XPS analyses were conducted at different electrochemical states, in conjunction with the structural and morphological characterization results discussed above. As shown in Figure 5a, a series of representative potential points was selected to cover the major capacity variation regions corresponding to different reaction states experienced during charge and discharge. With changes in electrode potential, the Raman spectra in the 1400–1600 cm^{-1} region, associated with ring-vibration modes of the TCNQ moiety, exhibit reversible intensity variations and slight peak shifts (Figure 5b), while the overall peak shapes remain unchanged and no new vibrational modes emerge. Two-dimensional Raman intensity contour maps (Figure 5c) further reveal that these spectral features evolve continuously and reversibly throughout the charge–discharge process, indicating that the electrochemical reaction primarily involves reversible evolution of electronic states within the donor–acceptor complex rather than destruction of molecular backbones or structural rearrangement. This interpretation is further supported by FT-IR results. As shown in Figure 5d, the –C≡N stretching vibration remains clearly observable at all electrochemical states, with the peak position remaining essentially unchanged and only reversible variations in absorption intensity detected, indicating that the TCNQ acceptor continuously participates in charge storage while maintaining stable chemical bonding. Taken together with the Raman analysis, these results support reversible electrochemical evolution of the donor–acceptor complex without inducing irreversible chemical structural changes. Ex situ XPS analysis provides additional insight into the evolution of chemical environments. As shown in Figure 5e, the relative intensities of C 1s components associated with C–N/C=N and –C≡N groups exhibit reversible changes at different electrochemical states, while the binding energy ranges remain unchanged, reflecting modulation of the local electronic environment during the reaction. Correspondingly, the N 1s spectra (Figure 5f) display similar reversible changes in nitrogen-related peak features, further supporting reversible donor–acceptor redox evolution during electrochemical operation, while the overall chemical bonding environment remains intact. In addition, the UV–vis spectrum of the post-cycling electrolyte (Figure S2) does not show obvious new absorption features, which is consistent with the absence of evident large-scale dissolution of active material under the present conditions. These results indicate that charge storage in PNZ–TCNQ under acidic aqueous conditions is associated with reversible redox evolution of the donor–acceptor complex, accompanied by the cooperative contribution of pseudocapacitive and diffusion-controlled processes, while preserving the structural stability of the charge-transfer assembly.

3.6. Schematic Illustration of the Construction and Mechanism of PNZ-TCNQ

Based on the combined results of structural characterization, electrochemical performance evaluation, kinetic analysis, and spectroscopic investigation at different electrochemical states, schematic illustrations of the charge-storage concept and working process of PNZ–TCNQ under acidic aqueous conditions were constructed (Figure 6a,b). As illustrated in Figure 6a, the PNZ donor and TCNQ acceptor form a charge-transfer solid-state assembly through intermolecular donor–acceptor interactions. This solid-state framework provides continuous pathways for reversible electron transport at the molecular scale and exhibits an overall dense structural feature. Furthermore, Figure 6b presents a schematic illustration of the electrochemical process of the organic charge-transfer complex (OCTC) under acidic aqueous conditions. During charge and discharge, electrochemical reactions are associated mainly with reversible redox evolution between donor–acceptor units within the complex framework, while the acidic aqueous envi-

ronment maintains overall charge balance. This process does not rely on pronounced long-range structural rearrangements but occurs while preserving the overall integrity of the charge-transfer complex, consistent with the reversible evolution of electronic environments revealed by Raman, FT-IR, and XPS analyses. These results demonstrate that the PNZ–TCNQ organic charge-transfer complex exhibits stable Faradaic behavior under acidic aqueous conditions, with charge storage governed by the cooperative contribution of pseudocapacitive and diffusion-influenced processes, thereby enabling stable capacity output over a wide range of operating conditions and extended cycling. This work provides a useful framework for understanding the electrochemical behavior of OCTC materials in acidic aqueous energy-storage systems and for the design and performance optimization of organic electrode materials through molecular and complex-structure engineering.

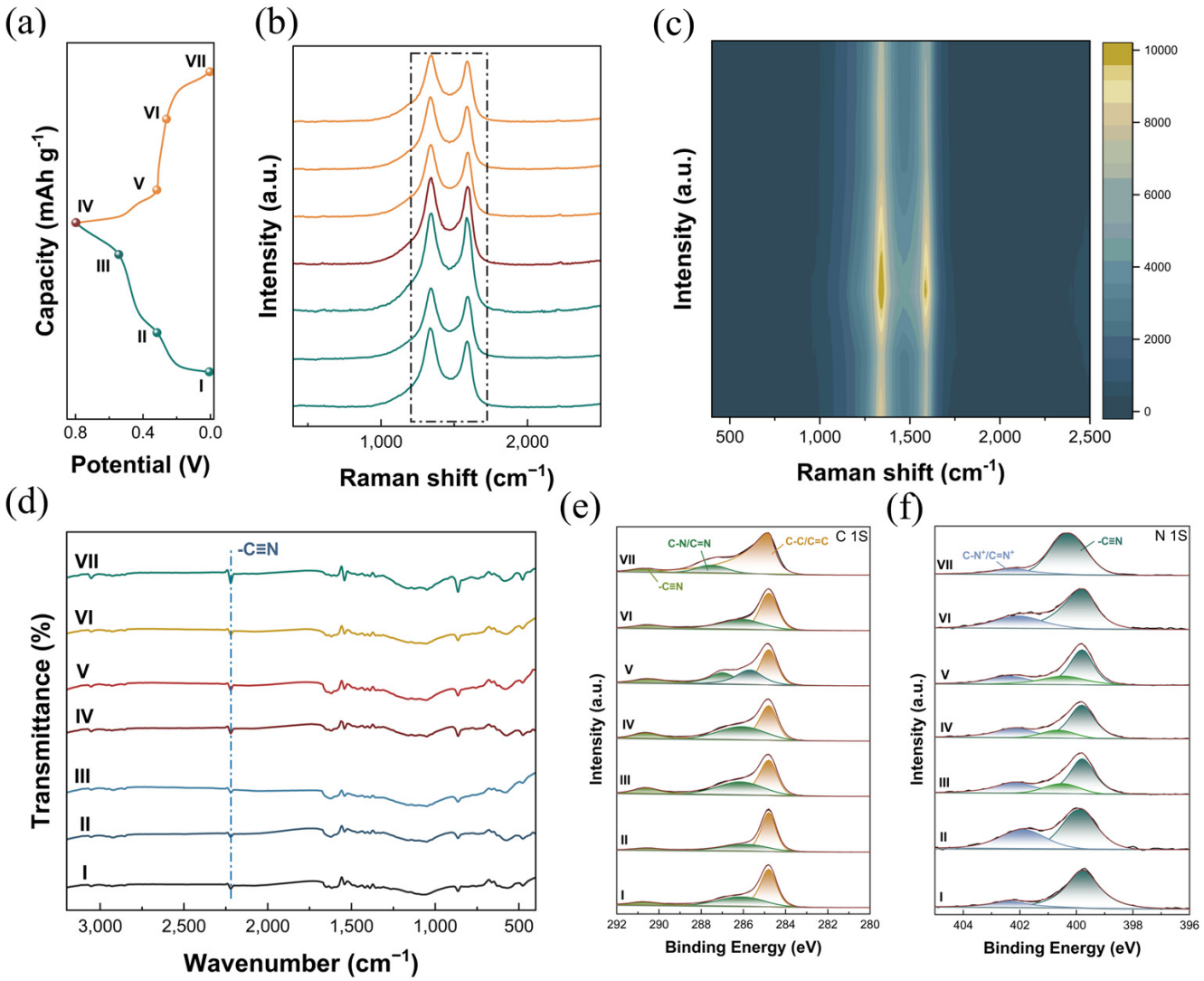

Figure 5. Storage performances of the PNZ-TCNQ: (**a**) Representative GCD profile of the PNZ-TCNQ electrode; (**b**,**c**) In situ Raman spectra and corresponding contour plots of the PNZ-TCNQ electrode; (**d**) Ex situ FT–IR spectra; (**e**,**f**) Ex situ XPS spectra.

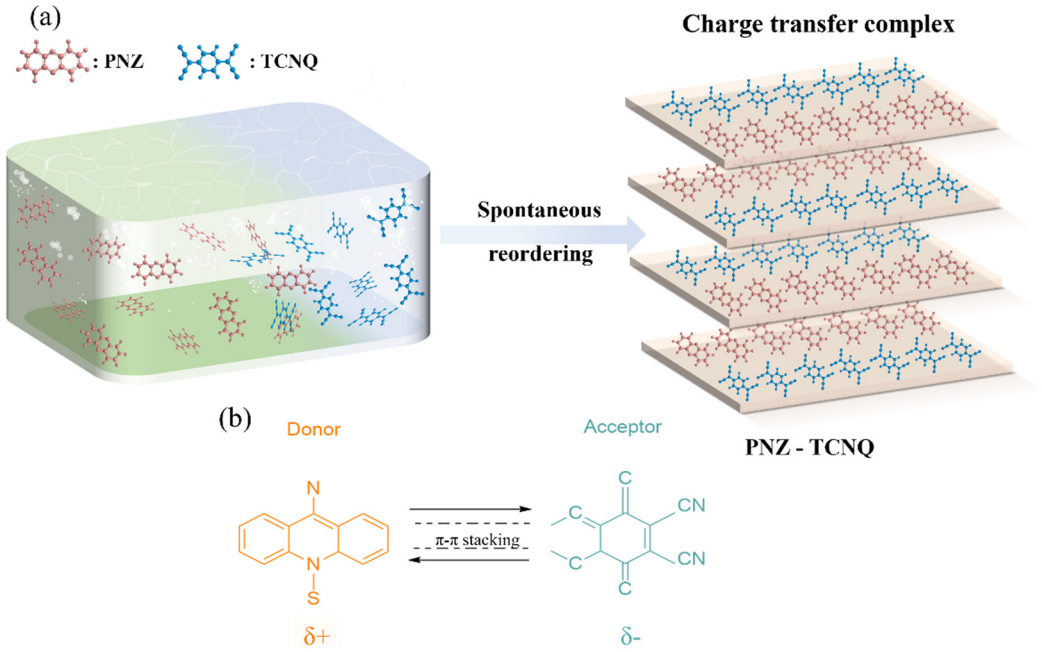

Figure 6. Concepts of PNZ-TCNQ: (**a**) Conceptual diagram of the OCTC PNZ–TCNQ; (**b**) Schematic diagram of working principles of the OCTC [40].

4. Conclusions

In summary, a PNZ–TCNQ organic charge-transfer complex was successfully constructed by regulating the complexation ratio between the PNZ donor and the TCNQ acceptor. Structural and morphological characterizations demonstrate that the molecular backbones remain intact during complex formation, leading to a dense solid-state charge-transfer structure that provides a stable structural basis for reversible electrochemical reactions under acidic aqueous conditions. Consequently, the PNZ–TCNQ complex exhibits stable and reproducible redox behavior in an acidic aqueous three-electrode system, accompanied by durable cycling performance. Notably, at a high current density of 5 A g^{-1}, the PNZ–TCNQ electrode sustains continuous operation for up to 10,000 cycles, with the discharge capacity remaining stable from an initial value of 65.8 mAh g^{-1} to approximately 56 mAh g^{-1}, demonstrating favorable electrochemical stability under long-term and high-rate operation. Further kinetic analysis combined with spectroscopic investigations at different electrochemical states reveals that charge storage in the PNZ–TCNQ complex is governed by the cooperative contribution of pseudocapacitive behavior and diffusion-influenced processes, which is associated with reversible redox evolution between donor–acceptor units. The intermolecular charge-transfer interaction plays an important role in maintaining efficient electronic transport while preserving structural stability during repeated cycling. These characteristics enable the PNZ–TCNQ organic charge-transfer complex to deliver stable electrochemical performance over a wide range of operating conditions. Overall, this work provides a useful strategy for designing organic charge-transfer complexes for acidic aqueous energy storage through control of molecular composition and complexation behavior. The insights gained from this study highlight the importance of intermolecular interaction regulation in governing electrochemical behavior and reaction kinetics, and offer guidance for the development of aqueous organic energy-storage materials with both fast kinetics and long-term cycling stability.

Supplementary Materials: The following supporting information can be downloaded at: https://www.mdpi.com/article/10.3390/coatings16040441/s1, Figure S1: Capacitive contribution analysis at different scan rates; Figure S2: UV–vis absorption spectrum of the electrolyte after 1000 cycles (fresh electrolyte as the blank); Figure S3: Galvanostatic charge–discharge curve of the electrode assembled with the PNZ:TCNQ = 1:1 material after 200 cycles at 0.6 A g^{-1}.

Author Contributions: Writing – original draft, X.S., X.Y., J.Y., W.Z. and P.S.; Visualization, J.Y. and W.Z.; Supervision, X.Y. and W.Z. All authors have read and agreed to the published version of the manuscript.

Funding: This research received no external funding.

Institutional Review Board Statement: Not applicable.

Informed Consent Statement: Not applicable.

Data Availability Statement: The original contributions presented in this study are included in the article/Supplementary Material. Further inquiries can be directed to the corresponding author.

Conflicts of Interest: The authors declare no conflict of interest.

References

1. Li, Y.; Song, J.; Yang, J. A Review on Structure Model and Energy System Design of Lithium-Ion Battery in Renewable Energy Vehicle. *Renew. Sustain. Energy Rev.* **2014**, *37*, 627–633. [CrossRef]
2. Lei, Y. Advanced Energy Materials Research: Key to Sustainable Energy Future. *Adv. Energy Mater.* **2025**, *16*, e04339. [CrossRef]
3. Zhang, W.; Zhang, F.; Ming, F.; Alshareef, H.N. Sodium-Ion Battery Anodes: Status and Future Trends. *EnergyChem* **2019**, *1*, 100012. [CrossRef]
4. Wu, X.; Dai, Y.; Li, N.W.; Chen, X.C.; Yu, L. Recent Progress in Ionic Liquid-Based Electrolytes for Nonaqueous and Aqueous Metal Batteries. *eScience* **2024**, *4*, 100173. [CrossRef]
5. Hu, Z.; Lin, L.; Jiang, Y.; Sun, L.; Liu, W.; Wang, Q.; Wang, F. Reveal the Source of Protons in Aqueous Hydrogen Proton Battery. *Energy Storage Mater.* **2024**, *73*, 103820. [CrossRef]
6. Zhang, L.; Zhang, C.; Berg, E.J. Mastering Proton Activities in Aqueous Batteries. *Adv. Mater.* **2024**, *37*, e2407852. [CrossRef]
7. Liang, G.; Mo, F.; Ji, X.; Zhi, C. Non-Metallic Charge Carriers for Aqueous Batteries. *Nat. Rev. Mater.* **2020**, *6*, 109–123. [CrossRef]
8. Wang, F.; Xu, K.; Wang, C. Charge Carrier Unveiled. *Nat. Sustain.* **2022**, *5*, 818–819. [CrossRef]
9. Schon, T.B.; McAllister, B.T.; Li, P.-F.; Seferos, D.S. The Rise of Organic Electrode Materials for Energy Storage. *Chem. Soc. Rev.* **2016**, *45*, 6345–6404. [CrossRef]
10. Qiao, J.-Q.; Zuo, S.-W.; Li, Z.-F.; Li, G. Latest Progress in Proton-Conducting Hydrogen-Bonded Organic Frameworks. *Inorg. Chem. Front.* **2023**, *10*, 5856–5884. [CrossRef]
11. Pal, S.C.; Mukherjee, D.; Sahoo, R.; Mondal, S.; Das, M.C. Proton-Conducting Hydrogen-Bonded Organic Frameworks. *ACS Energy Lett.* **2021**, *6*, 4431–4453. [CrossRef]
12. Song, Z.; Miao, L.; Ruhlmann, L.; Lv, Y.; Li, L.; Gan, L.; Liu, M. Proton-Conductive Supramolecular Hydrogen-Bonded Organic Superstructures for High-Performance Zinc-Organic Batteries. *Angew. Chem. Int. Ed.* **2023**, *62*, e202219136. [CrossRef] [PubMed]
13. Ogawa, T.; Ohashi, H.; Tamaki, T.; Yamaguchi, T. Proton Diffusion Facilitated by Indirect Interactions Between Proton Donors Through Several Hydrogen Bonds. *Chem. Phys. Lett.* **2019**, *731*, 136627. [CrossRef]
14. Sun, Y.; Wei, J.; Fu, Z.; Zhang, M.; Zhao, S.; Xu, G.; Li, C.; Zhang, J.; Zhou, T. Bio-Inspired Synthetic Hydrogen-Bonded Organic Frameworks for Efficient Proton Conduction. *Adv. Mater.* **2022**, *35*, 2208625. [CrossRef] [PubMed]
15. Arsenault, E.A.; Guerra, W.D.; Shee, J.; Cruz, E.A.R.; Yoneda, Y.; Wadsworth, B.L.; Odella, E.; Urrutia, M.N.; Kodis, G.; Moore, G.F.; et al. Concerted Electron-Nuclear Motion in Proton-Coupled Electron Transfer-Driven Grotthuss-Type Proton Translocation. *J. Phys. Chem. Lett.* **2022**, *13*, 4479–4485. [CrossRef]
16. Zuo, D.; Tian, G.; Li, X.; Chen, D.; Shu, K. Recent Progress in Surface Coating of Cathode Materials for Lithium Ion Secondary Batteries. *J. Alloys Compd.* **2017**, *706*, 24–40. [CrossRef]
17. Li, W.; Song, Q.; Dong, Q.; Zhang, J.; Wang, J.; Wu, Y.; Yu, Y.; Li, X. Proton Storage Chemistry in Aqueous Zinc-Inorganic Batteries with Moderate Electrolytes. *Adv. Mater.* **2024**, *37*, 2414019. [CrossRef]
18. Fu, L.; Wang, X.; Zhang, R.; Li, R.; Wei, G.; Li, M. Proton Co-Intercalation Enabled High-Performance Aqueous Multivalent Metal-Ion Batteries. *J. Mater. Chem. A* **2025**, *13*, 24300–24319. [CrossRef]
19. Yue, F.; Tie, Z.; Deng, S.; Wang, S.; Yang, M.; Niu, Z. An Ultralow Temperature Aqueous Battery with Proton Chemistry. *Angew. Chem. Int. Ed.* **2021**, *60*, 13882–13886. [CrossRef]

20. Wang, Y.; Wang, C.; Wang, W.; Zhang, Y.; Guo, Z.; Huang, J.; Yan, L.; Ma, J.; Wang, Y. Organic Hydronium-Ion Battery with Ultralong Life. *ACS Energy Lett.* **2023**, *8*, 1390–1396. [CrossRef]
21. Zhu, Y.; Yang, X.; Zhang, X. Hydronium Ion Batteries: A Sustainable Energy Storage Solution. *Angew. Chem. Int. Ed.* **2017**, *56*, 6378–6380. [CrossRef] [PubMed]
22. Liu, J.; Guo, K.; Guo, W.; Chang, J.; Li, Y.; Bao, F. Superconjugated Anthraquinone Carbonyl-Based Covalent Organic Framework as Anode Material for High-Performance Aqueous Ammonium-Ion Batteries. *Angew. Chem. Int. Ed.* **2025**, *64*, e202424494. [CrossRef] [PubMed]
23. Lu, C.; Zhao, F.; Tao, B.; Wang, Z.; Wang, Y.; Sheng, J.; Tang, G.; Wang, Y.; Guo, X.; Li, J.; et al. Anode-Free Aqueous Aluminum Ion Batteries. *Small* **2024**, *20*, 2402025. [CrossRef] [PubMed]
24. Wang, H.; Wu, J.; Zheng, Z.; Qin, J.; Guo, Z.; Zhang, Z.; Wen, W. Surface Anion Effects in Aqueous Hydrogen Ion Batteries. *J. Electron. Mater.* **2024**, *53*, 3474–3481. [CrossRef]
25. Han, W.; Li, M.; Ma, Y.; Yang, J. Dianhydride-Based Polyimide as Organic Electrode Materials for Aqueous Hydronium-Ion Battery. *Electrochim. Acta* **2022**, *403*, 139550. [CrossRef]
26. Ma, Y.; Wei, Y.; Han, W.; Tong, Y.; Song, A.J.; Zhang, J.; Li, H.; Li, X.; Yang, J. Proton Intercalation/De-Intercalation Chemistry in Phenazine-Based Anode for Hydronium-Ion Batteries. *Angew. Chem. Int. Ed.* **2023**, *62*, e202314259. [CrossRef]
27. Deng, X.; Sarpong, J.K.; Zhang, G.; Hao, J.; Zhao, X.; Li, L.; Li, H.; Han, C.; Li, B. Proton Storage Chemistry in Aqueous Zinc-Organic Batteries: A Review. *InfoMat* **2022**, *5*, e12382. [CrossRef]
28. Hurlbutt, K.; Wheeler, S.; Capone, I.; Pasta, M. Prussian Blue Analogs as Battery Materials. *Joule* **2018**, *2*, 1950–1960. [CrossRef]
29. Li, Y.; Zhao, J.; Hu, Q.; Hao, T.; Cao, H.; Huang, X.; Liu, Y.; Zhang, Y.; Lin, D.; Tang, Y.; et al. Prussian Blue Analogs Cathodes for Aqueous Zinc Ion Batteries. *Mater. Today Energy* **2022**, *29*, 101095. [CrossRef]
30. Qiu, S.; Xu, Y.; Wu, X.; Ji, X. Prussian Blue Analogues as Electrodes for Aqueous Monovalent Ion Batteries. *Electrochem. Energy Rev.* **2021**, *5*, 242–262. [CrossRef]
31. An, S.; Hu, L.; Li, X.; Zhao, S.; Shi, M.; Yan, C. A Solid-Diffusion-Free Hydronium-Ion Battery with Ultra-Long Cycle Life over 8000 Cycles. *Energy Storage Mater.* **2024**, *64*, 103076. [CrossRef]
32. Chen, W.; Chen, T.; Fu, J. Pivotal Role of Organic Materials in Aqueous Zinc-Based Batteries: Regulating Cathode, Anode, Electrolyte, and Separator. *Adv. Funct. Mater.* **2023**, *34*, 2308015. [CrossRef]
33. Yang, G.; Zhu, Y.; Hao, Z.; Lu, Y.; Zhao, Q.; Zhang, K.; Chen, J. Organic Electroactive Materials for Aqueous Redox Flow Batteries. *Adv. Mater.* **2023**, *35*, 2301898. [CrossRef]
34. Hu, C.; Lu, Y.; Gu, H.; Zhang, W.; Li, Z. Multiple Redox Site π-Conjugated Materials for Aqueous Aluminum–Organic Battery Cathodes. *ACS Energy Lett.* **2024**, *9*, 4353–4360. [CrossRef]
35. Goetz, K.P.; Vermeulen, D.; Payne, M.E.; Kloc, C.; McNeil, L.E.; Jurchescu, O.D. Charge-Transfer Complexes: New Perspectives on an Old Class of Compounds. *J. Mater. Chem. C* **2014**, *2*, 3065–3076. [CrossRef]
36. Horiuchi, S.; Okimoto, Y.; Kumai, R.; Tokura, Y. Quantum Phase Transition in Organic Charge-Transfer Complexes. *Science* **2003**, *299*, 229–232. [CrossRef] [PubMed]
37. Madhu, M.; Ramakrishnan, R.; Vijay, V.; Hariharan, M. Free Charge Carriers in Homo-Sorted π-Stacks of Donor–Acceptor Conjugates. *Chem. Rev.* **2021**, *121*, 8234–8284. [CrossRef]
38. Yamane, H.; Kosugi, N. High Hole-Mobility Molecular Layer Made from Strong Electron Acceptor Molecules with Metal Adatoms. *J. Phys. Chem. Lett.* **2017**, *8*, 5366–5371. [CrossRef]
39. Denis, P.A. Band Gap Opening in Bilayer Graphene by the Simultaneous Adsorption of Electron Donating and Electron Acceptor Molecules. *Comput. Theor. Chem.* **2017**, *1120*, 96–101. [CrossRef]
40. Lee, S.; Hong, J.; Jung, S.-K.; Ku, K.; Kwon, G.; Seong, W.M.; Kim, H.; Yoon, G.; Kang, I.; Hong, K.; et al. Charge-Transfer Complexes for High-Power Organic Rechargeable Batteries. *Energy Storage Mater.* **2019**, *20*, 462–469. [CrossRef]
41. Lee, S.; Kim, J.; Hong, J.; Kang, K. Unlocking the Full Redox Capability of Organic Charge-Transfer Complex in High-Loading Electrodes for Organic Rechargeable Batteries. *Adv. Energy Mater.* **2024**, *15*, 2404116. [CrossRef]
42. Katkar, P.K.; Naikwade, M.B.; Lee, S.-W. A Synergistic Electrochemical Properties of 3D Marigold-like Fe-Cu-Ag Phosphate/MWCNTs Nanocomposite towards Hybrid Solid-State Supercapatteries. *J. Alloys Compd.* **2025**, *1038*, 182815. [CrossRef]

Disclaimer/Publisher's Note: The statements, opinions and data contained in all publications are solely those of the individual author(s) and contributor(s) and not of MDPI and/or the editor(s). MDPI and/or the editor(s) disclaim responsibility for any injury to people or property resulting from any ideas, methods, instructions or products referred to in the content.